

Density and viscosity of a polyol ester lubricant: Measurement and molecular dynamics simulation

Lingnan Lin*, Mark A. Kedzierski

National Institute of Standards and Technology, 100 Bureau Drive, Gaithersburg, MD 20899, USA

ARTICLE INFO

Article history:

Received 6 March 2020

Revised 29 June 2020

Accepted 7 July 2020

Available online 9 July 2020

Keywords:

Molecular simulation

POE oil

NEMD

Transport property

Lubrication

Rheology

ABSTRACT

This paper presents new experimental data and detailed molecular dynamics (MD) simulations of density and viscosity for a typical, pure polyol ester, pentaerythritol tetrahexanoate (PEC6). The density and Newtonian viscosity of PEC6 were measured over 258.15 K to 373.15 K at atmospheric pressure and predicted by MD for the same temperature range and a wide range of pressure (0.1 MPa to 1 GPa). The viscosity was calculated primarily by nonequilibrium molecular dynamics (NEMD), while equilibrium molecular dynamics (EMD) simulations were also performed for comparison. In NEMD, the Newtonian viscosity was obtained by fitting the shear viscosities at different strain rates (10^7 s^{-1} to 10^{10} s^{-1}) computed by NEMD simulations to a rheological model (Eyring or Carreau). Three force fields (OPLS, LOPLS, and DREIDING) were benchmarked in terms of their density and viscosity prediction accuracy of PEC6. The predictions were compared with the present measurements for 0.1 MPa and literature data for high pressures. Overall, LOPLS is the most accurate force field for PEC6. It predicts the density of PEC6 to within $\pm 3\%$, and Newtonian viscosity to within 50% for the range of simulation conditions. The LOPLS force field and the presented computation techniques are expected to apply to other polyol esters and perhaps other classes of lubricants.

Published by Elsevier Ltd.

Densité et viscosité d'un lubrifiant à base d'ester de polyol: Mesurage et simulation de la dynamique moléculaire

Mots-clés: Simulation moléculaire; Huile POE; Dynamique moléculaire en état de non-équilibre; Propriété de transport; Lubrification; Rhéologie

1. Introduction

The performance, efficiency, and longevity of a refrigeration compressor are closely related to how well the mechanical moving parts of the compressor, such as pistons, rotors, valves, connecting rods and cranks, are lubricated (Marsh and Kandil, 2002; Youbi-Idrissi et al., 2003). Compressor lubrication is achieved by interposing a lubricant film between moving surfaces that reduces or eliminates direct solid-to-solid contact. Besides this primary function, refrigeration lubricants have several secondary functions such as heat dissipation, sealing, corrosion protection, debris suspension, etc. Consequently, the multiple roles that lubricants play, and

the broad operating range of temperatures and pressures, demand an adequate knowledge of the properties of refrigeration lubricants for proper selection and design.

Viscosity and density are two of the most important properties of a lubricant, because they are inherently linked to the lubricant hydrodynamics (Ewen et al., 2016). In a compressor, lubricated machine components, such as bearings, generally operate in elastohydrodynamic lubrication (EHL) regime where lubricants are compressed in concentrated contacts and the pressure is extremely high (up to giga-pascals). The thickness of a lubricant film is a function of the viscosity and its dependences with pressure and temperature (Bair, 2019a), which has a fundamental impact on the equipment performance and reliability. A decrease of viscosity will cause thinning of the lubricant film and may cause equipment failure if the viscosity is too low, while an excessively large viscosity can lead to increased motor loading and higher power

* Corresponding author.

E-mail address: lingnan.lin@nist.gov (L. Lin).

Nomenclature

English symbols

F	force
<i>m</i>	mass
P	stress tensor
p	momentum
<i>p</i>	pressure
<i>q</i>	partial charge
r	position
<i>r</i>	bond length
<i>T</i>	temperature
<i>U</i>	energy, uncertainty
<i>V</i>	volume

Greek symbols

$\dot{\gamma}$	shear rate
$\dot{\gamma}_c$	critical shear rate
η	shear viscosity
η_N	Newtonian viscosity
θ	bond angle
ν	kinematic viscosity
ρ	density
σ_E	Eyring stress
τ	characteristic time
ϕ	proper dihedral angle
χ	improper dihedral angle

Abbreviation

EHL	elastohydrodynamic lubrication
EMD	equilibrium molecular dynamics
MD	molecular dynamics
NEMD	non-equilibrium molecular dynamics
PEC6	pentaerythritol tetrahexanoate
POE	polyol ester

consumption (Michels and Sienel, 2003). These characteristics are paramount considerations when choosing the viscosity grade of a lubricant. At present, the research on refrigeration lubricants relies heavily upon experimental data and correlation. Unfortunately, the data are very limited, especially for giga-pascal pressure where measurements are difficult to perform. This makes lubricant development heavily reliant upon experience and intuition as well as on costly trial-and-error experimentation. To select and design lubricants in a more cost-effective manner, reliable methods for predicting viscosity and density are needed.

In recent years, molecular dynamics (MD) simulation has been used to complement experimentation and to study thermodynamic and transport properties. A MD simulation involves the construction of a model that calculates the potential energy of the molecular system as a function of its configuration and molecular structure, i.e., molecular model or force field. In general, the degree to which a MD prediction agrees with the experiment mainly depends on the accuracy of the force field. Given a force field, a collection of atoms is maintained at a particular state during which an atomistic trajectory (i.e., time evolution of position and momenta) is generated. The thermodynamic and transport properties can be derived from the resultant trajectory using a calculation method based on statistical mechanics. The selection of the calculation method and how the method is implemented also have an impact on the accuracy of the MD prediction, and play a key role in the computational efficiency. In summary, accurate and efficient MD simulations entail two key elements: a good force field and an optimal implementation of the property calculation.

There have been a variety of force fields developed for different purposes, and some of them have been successfully used to model the viscosity of lubricants. Kioupis and Maginn (1999a, 1999b) used the TraPPE united-atom force field (Martin and Siepmann, 1998) to model hydrocarbon lubricants (n-hexane/n-hexadecane mixtures) and poly- α -olefin (PAO) lubricants, and used equilibrium molecular dynamics (EMD) and non-equilibrium molecular dynamics (NEMD) methods to compute viscosity. McCabe et al. (2001) used a united-atom force field (Mondello et al., 1996; Siepmann et al., 1993) to study the viscosity-temperature dependence of an alkane lubricant (9-octylheptadecane). The same force field was subsequently used to study another lubricant: 1-decene trimer (Liu et al., 2015). Ewen et al. (2016) benchmarked the accuracy of density and viscosity predictions for a large number of united-atom and all-atom force fields. They used EMD to simulate n-hexadecane, and found that all-atom force fields yielded better prediction for long-chain, linear lubricants. Recently, Jadhao and Robbins (2017, 2019) presented detailed NEMD simulation results of a model EHL fluid, squalene, over a wide range of temperature and pressure. However, studies on refrigeration lubricants such as polyol ester (POE) are rarely found in the literature. POE lubricants feature one or more ester groups in a molecule as well as long and branched molecular architecture, which differs significantly from and is more complex than other lubricants. Thus, the applicability of the existing force fields needs to be verified for POE lubricants with a benchmark evaluation.

In this study, molecular dynamics simulation is employed to predict the density and viscosity of a POE refrigeration lubricant over a wide range of temperature (258 K to 373 K) and pressure (0.1 MPa to 1 GPa). Different force fields and models are evaluated to establish an optimal protocol for calculating the viscosity of POE lubricants. The density and viscosity of the lubricant are measured for comparison. Methodology details of the measurement and the simulation are illustrated in Section 2 and Section 3, respectively. Experimental and simulation results are given in Section 4 and Section 5, respectively. At last, discussion and conclusions are presented Section 6 and Section 7, respectively.

2. Material and measurements

Polyol esters are the condensation product of a polyol (i.e., an alcohol with multiple hydroxyl groups) and carboxylic acids. A commercial POE lubricant contains not only polyol esters as the base stock but also various additives for performance modification, which makes its molecular structure and composition difficult to define and thereby complicates the modeling and simulation. For this reason, pure polyol ester lubricants with relatively simple molecular structures are commonly studied (Bobbo et al., 2008; Wang et al., 2015). In this study, we choose a pure polyol ester, pentaerythritol tetrahexanoate (PEC6, $C_{29}H_{52}O_8$, CAS No. 7445-47-8) because it has a typical molecular structure of POE lubricants and is a common component of many commercial lubricants. The chemical structure of PEC6 is shown in Fig. 1(a) and (b). The manufacture-quoted purity of the tested PEC6 was $(95 \pm 2)\%$ based on the proton nuclear magnetic resonance (1H NMR).

A Stabinger-type viscometer was used to measure the density and the viscosity¹ of the lubricant over a temperature range from 258.15 K to 373.15 K. The operation principle of the Stabinger viscometer relies on rotating concentric cylinders. The liquid sample is contained in the annulus of a concentric cylinder where the inner cylinder is hollow and of less mass than the sample.

¹ The “viscosity” herein refers to dynamic viscosity [mPa·s] unless otherwise stated.

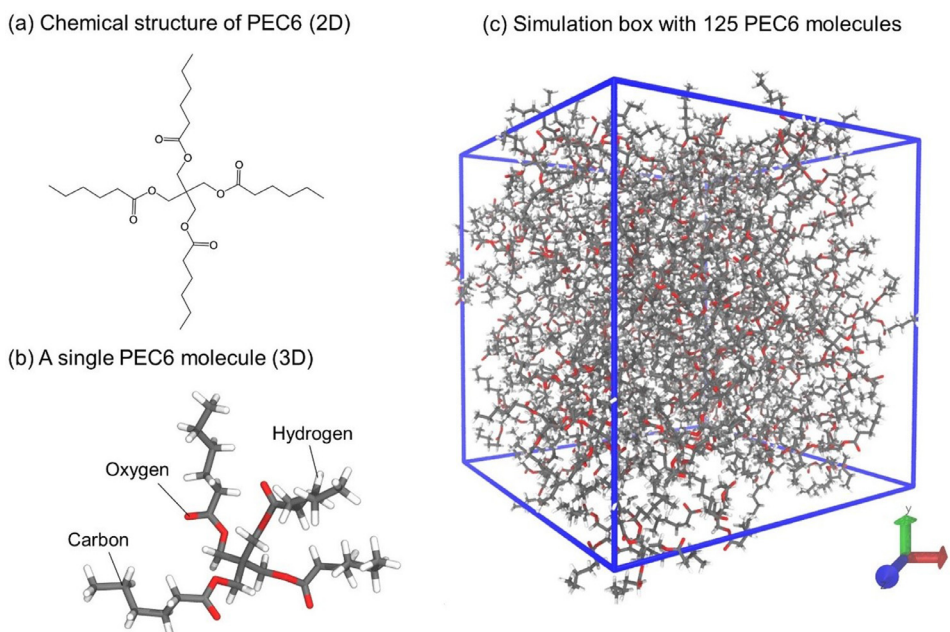


Fig. 1. Molecular structure of PEC6 (a and b) and the molecular dynamics simulation box with 125 PEC6 molecules in a perspective view (c).

This allows the inner cylinder to float freely and be centered by centrifugal forces in the sample when the outer cylinder is spun by a rotating magnetic field. Viscous shear forces on the liquid transfer the rotation to the inner cylinder. Measurements on the inner cylinder are used to calculate the difference in speed and torque between the outer and inner cylinder, and thus, the dynamic viscosity. All calculations are internal to the instrument. The viscometer operates at low shear rates, and therefore, the measured viscosity is in the Newtonian regime (Kedzierski et al., 2017). Measurements were made by stepping up the temperature at an interval of 5 K. Three repeated runs were carried out on the same day, producing 72 measurements for density and viscosity. The temperature range covers common refrigeration compressor conditions. The measurements were made at ambient pressure (100.84 kPa) at an approximate altitude of 137 m above sea level (Gaithersburg, Maryland, USA). The uncertainties of the density and the viscosity for a 95% confidence level were calculated to be $\pm 0.1\%$ and $\pm 2.1\%$, respectively. More details about the density and viscosity measurement are provided in Refs (Kedzierski, 2013, 2012; Kedzierski et al., 2017).

3. Molecular dynamics simulation

Molecular dynamics (MD) is essentially the simulation of the time evolution of atomistic positions (i.e., trajectory) of a molecular system. This is done by integrating the Newton's equations of motion for every atom in the system:

$$m_i \frac{d^2}{dt^2} \mathbf{r}_i = \mathbf{F}_i \quad (1)$$

where m_i , \mathbf{r}_i , and \mathbf{F}_i are mass, position and force of the atom i , respectively. The force term is calculated from the potential energy $U_{pe}(\mathbf{r}_1, \mathbf{r}_2, \dots, \mathbf{r}_N)$:

$$\mathbf{F}_i = -\frac{\partial}{\partial \mathbf{r}_i} U_{pe}(\mathbf{r}_1, \mathbf{r}_2, \dots, \mathbf{r}_N) \quad (2)$$

The force field is used here to determine the potential energy U_{pe} . With the trajectory generated by MD simulation, properties like density and viscosity can be derived.

3.1. Force field

The force field is basically a set of functions and parameters that are used to model the interactions in the molecular system. The total potential energy of a molecular system can be expressed by the sum of the molecular energy components:

$$U_{pe} = U_{elec} + U_{vdw} + U_{bond} + U_{angle} + U_{torsion} + U_{improper} \quad (3)$$

where U_{elec} and U_{vdw} represent non-bonded interactions of electrostatic interaction and van der Waals interaction, respectively; U_{bond} , U_{angle} , $U_{torsion}$, $U_{improper}$ represent bonded interactions corresponding to contributions of bond stretching, angle bending, internal rotation around the dihedral angle (torsion), and out-of-plane bending (improper torsion), respectively.

Our study started with the all-atom force field OPLS (Jorgensen et al., 1996; Robertson et al., 2015), because it's one of the most popular force fields for organic liquids and, more importantly, it has been used to predict the vapor liquid equilibrium (VLE) of the PEC6/CO₂ system and the prediction agreed well with experiments (Sugii et al., 2015). The potential functions used by OPLS are:

$$\begin{cases} U_{elec} = \frac{1}{4\pi\epsilon_0} \frac{q_i q_j}{r_{ij}} \\ U_{vdw} = 4\epsilon_{ij} \left[\left(\frac{\sigma_{ij}}{r_{ij}} \right)^{12} - \left(\frac{\sigma_{ij}}{r_{ij}} \right)^6 \right] \\ U_{bond} = K_r (r - r_0)^2 \\ U_{angle} = K_\theta (\theta - \theta_0)^2 \\ U_{torsion} = \frac{V_1}{2} [1 + \cos(\phi)] + \frac{V_2}{2} [1 - \cos(2\phi)] + \frac{V_3}{2} [1 + \cos(3\phi)] \\ U_{improper} = K_\chi (\chi - \chi_0)^2 \end{cases} \quad (4)$$

where r , θ , ϕ , and χ are bond length, bond angle, proper dihedral angle, and improper dihedral angle, respectively; K_r , r_0 , K_θ , θ_0 , V_1 , V_2 , V_3 , K_χ , χ_0 , ϵ_{ij} , σ_{ij} are force field parameters; q is partial charge. The parameters of the OPLS are given in Appendix A. An extension force field of OPLS, named LOPLS (Pluhackova et al., 2015; Siu et al., 2012), was also studied here because it was optimized for long hydrocarbons and small esters. Following the framework of the OPLS parametrization, LOPLS refines a few torsional parameters and adjusts some non-bonded parameters. The

parameters of LOPLS are given in Appendix B. In addition to OPLS and LOPLS, a generic force field named DREIDING (Mayo et al., 1990) was tested for comparison. DREIDING uses a different torsional potential: $U_{\text{torsion}} = K_{\phi}[1 + d \cos(n\phi)]$ where K_{ϕ} , d , and n are parameters, while the functional forms for other interactions are the same as those of OPLS and LOPLS. The parameters of DREIDING are given in Appendix C.

3.2. Density model

To calculate the density, the molecules were maintained at an equilibrium state in a box in an isothermal–isobaric ensemble (NPT). The density was calculated by:

$$\rho = \frac{\sum m_i}{\langle V \rangle} \quad (5)$$

where $\sum m_i$ is the total mass of the atoms, V is the simulation box volume, and the angle bracket in Eq. (5) denotes equilibrium ensemble average (time average).

3.3. Viscosity model

Equilibrium molecular dynamics (EMD) and non-equilibrium molecular dynamics (NEMD) methods are the two main classes of methods for calculating viscosity. EMD methods sample the time-dependence of thermal fluctuations in the stress tensors, which can be related to viscosity using the Green-Kubo formula or the Einstein relation (Frenkel and Smit, 2002). In NEMD, an external field (perturbation) is applied to the equations of motion and the response of the system at non-equilibrium steady state is sampled to obtain the viscosity. Theoretically, EMD and NEMD methods can yield equivalent results, but in practice they are subject to different statistical error and computational cost, depending on the viscosity or the molecular size and complexity. EMD works best for low viscosity fluids, typically less than 20 mPa·s, while it becomes extremely computationally expensive for viscosity higher than 50 mPa·s (Maginn et al., 2019). The reason is that EMD requires a simulation time at least multiple of the molecule's relaxation time to obtain statistically meaningful result. High viscosities are associated with long relaxation time and thus require long simulation time that may not be accessible to current computers. Too long a simulation time may also cause the accumulation of thermal noise and poor convergence (Chen et al., 2009; Hess, 2002). NEMD, on the other hand, is often preferred for large molecules with high viscosity (McCabe et al., 2002). Ewen et al. (2016) suggested that NEMD is more suitable for predicting viscosity for chain-lengths greater than C_{16} . Considering that the PEC6 lubricant is a relatively large, complex molecule that has 29 carbon atoms and four ester chains, and its viscosity range from approximately 3 mPa·s to 500 mPa·s for the investigated temperatures (see Fig. 4), NEMD was used as the primary method while EMD was used as the secondary for selected conditions for comparison and validation. The models of both methods are briefly illustrated in the following.

- Nonequilibrium molecular dynamics (NEMD) simulations

In NEMD simulations, a planar Couette flow was set up by continuously deforming the system with a constant strain rate using the SLLOD equations of motion (Evans and Morriss, 2008), as shown in Fig. 2(b). The volume was fixed and the temperature was maintained constant with the Nose/Hover thermostat (Hoover, 1985). The dynamics viscosity (or shear viscosity) η was calculated by the stress tensor:

$$\eta(\dot{\gamma}) = -\frac{\langle P_{xy} \rangle}{\dot{\gamma}} \quad (6)$$

where P_{xy} is the xy component of the stress tensor, $\dot{\gamma}$ is the shear strain rate: $\dot{\gamma} = \partial u_x / \partial y$ (i.e., the gradient of the streaming velocity

at flow direction, u_x , along the y axis). The stress tensor \mathbf{P} is given by the virial theorem:

$$\mathbf{P}\mathbf{V} = \sum_i \frac{\mathbf{p}_i \mathbf{p}_i}{m_i} + \sum_i \mathbf{r}_i \mathbf{F}_i \quad (7)$$

where \mathbf{p}_i is the momentum of atom i , m_i is the mass, \mathbf{r}_i is the position vector, and \mathbf{F}_i is the force acting on the atom. Note that the shear viscosity $\eta(\dot{\gamma})$ computed from Eq. (6) is shear-rate-dependent. For low $\dot{\gamma}$, $\eta(\dot{\gamma})$ remains a constant equal to the Newtonian viscosity η_N ; for $\dot{\gamma} > \dot{\gamma}_c$ ($\dot{\gamma}_c$ is the critical point where the fluid transitions from Newtonian to non-Newtonian), $\eta(\dot{\gamma})$ changes with the increase of $\dot{\gamma}$.

Our goal is to obtain η_N . A common problem to compute η_N from $\eta(\dot{\gamma})$ is that the thermal noise in the NEMD simulation becomes increasingly significant as $\dot{\gamma}$ decreases, especially when $\dot{\gamma} < \dot{\gamma}_c$, leading to a nonlinearly increased computing uncertainty of $\eta(\dot{\gamma})$ or the simulation time required to achieve a desired uncertainty (McCabe et al., 2002). For acceptable uncertainty, the lowest accessible $\dot{\gamma}$ is typically 10^5 s^{-1} to 10^8 s^{-1} depending on the individual system (Jadhao and Robbins, 2017; Lu et al., 2019). This means we can't simply compute $\eta(\dot{\gamma})$ for a low $\dot{\gamma}$ near zero to directly obtain η_N . On the other hand, it's very difficult to precisely determine $\dot{\gamma}_c$ a priori, hence it's also impractical to obtain η_N directly from $\eta(\dot{\gamma})$ by one simulation for $\dot{\gamma}_c$ or for a $\dot{\gamma}$ that happens to fall into the Newtonian regime ($\dot{\gamma} < \dot{\gamma}_c$). Therefore, NEMD simulations were carried out for a series of $\dot{\gamma}$, and the η_N were obtained by fitting the $\eta(\dot{\gamma})$ to a rheological model that computes viscosity as a function of shear rate.

Two rheological models are studied, i.e., the Eyring model (Ewell and Eyring, 1937; Eyring, 1936) and the Carreau model (Carreau, 1972). The Eyring model assumes that the shear flow is a thermally activated process and there is only one activation energy barrier with a single characteristic height for the shear to occur. The equation for the Eyring model is:

$$\dot{\gamma} = \frac{\sigma_E}{\eta_N} \sinh \left(\frac{\langle P_{xy} \rangle}{\sigma_E} \right) \quad (8)$$

where σ_E and η_N are the Eyring stress and the Newtonian viscosity, respectively. Eq. (8) can be rewritten in an explicit form of η :

$$\eta = \frac{\eta_N}{\tau \dot{\gamma}} \ln \left(\tau \dot{\gamma} + \sqrt{(\tau \dot{\gamma})^2 + 1} \right) \quad (9)$$

where $\tau = \eta_N / \sigma_E$ is the characteristic time. Carreau model, on the other hand, assumes there is a wide range of energy barrier heights. The Carreau equation is:

$$\eta = \eta_N [1 + (\tau \dot{\gamma})^2]^{(n-1)/2} \quad (10)$$

where τ is the characteristic time and n is the power-law exponent. Note that for both models the shear-thinning occurs at the critical shear rate $\dot{\gamma}_c = 1/\tau$.

- Equilibrium molecular dynamics (EMD) simulations

For the EMD simulations, the shape of the simulation box was fixed (see Fig. 2(a)), and the viscosity was correlated to the ensemble average of the autocorrelation of the stress tensor at a fully equilibrated state. Here, the improved Green-Kubo relation was used to calculate the Newtonian viscosity (Cui et al., 1998a; Daivis and Evans, 1994):

$$\eta_N = \frac{V}{10k_B T} \int_0^\infty \left\langle \sum_{\alpha\beta} P_{\alpha\beta}^{\text{pos}}(0) P_{\alpha\beta}^{\text{pos}}(t) \right\rangle dt \quad (11)$$

Therein, V is the volume, k_B is the Boltzmann constant, T is the temperature, and $P_{\alpha\beta}^{\text{pos}}(0) P_{\alpha\beta}^{\text{pos}}(t)$ is the autocorrelation function of $P_{\alpha\beta}^{\text{pos}}$. $P_{\alpha\beta}^{\text{pos}}$ is $\alpha\beta$ elements of the traceless symmetric part of the

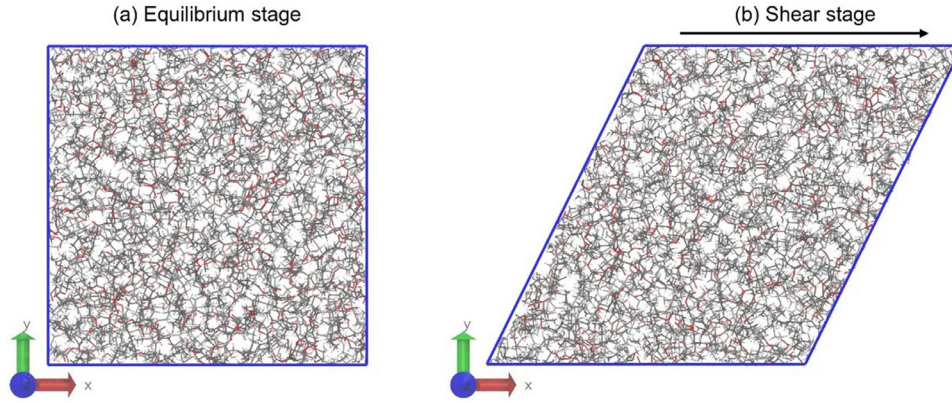


Fig. 2. Snapshots of the MD simulations at equilibrium stage (a) and shearing stage (b).

stress tensor ($\alpha\beta$ represents any pair of distinct Cartesian coordinates x , y and z), given by

$$P_{\alpha\beta}^{\text{os}} = \frac{1}{2} (P_{\alpha\beta} + P_{\beta\alpha}) - \frac{1}{3} \delta_{\alpha\beta} \sum_y P_{yy} \quad (12)$$

where $\delta_{\alpha\beta}$ is the Kronecker delta function ($\delta_{\alpha\beta} = 1$ for $\alpha = \beta$; $\delta_{\alpha\beta} = 0$ for $\alpha \neq \beta$), $P_{\alpha\beta}$ is the elements of the stress tensor \mathbf{P} , as calculated by Eq. (7).

Note that Eq. (11) makes use of all elements of the stress tensor (i.e., both diagonal and off-diagonal elements), and this can provide smaller statistical errors than using the original Green-Kubo relation, which uses only the off-diagonal elements of the stress tensor. In addition, the viscosity calculated by the EMD simulations (Eq. (11)) is theoretically equivalent to the low-shear viscosity of NEMD simulations.

3.4. Simulation details

MD simulations were performed using the LAMMPS package (Plimpton, 1995) for temperature from 258 K to 373 K and pressure from 0.1 MPa to 1 GPa. LAMMPS data files that contain the information of molecular topology, force field parameters, etc., were prepared using Moltemplate (Jewett, 2019). Force field parameters were manually checked to ensure that the values are in accordance with those in the literature of origin. The simulations were conducted in cubic boxes with periodic boundary conditions in all directions. The standard velocity-Verlet algorithm (Verlet, 1967) was used to integrate the equations of motion with a timestep of 0.5 fs. A total of 125 molecules (125×89 atoms) were used in all simulations (see Fig. 1(c)). The Nosé–Hoover thermostat (Hoover, 1985) and the extended Lagrangian approach (Shinoda et al., 2004) were applied to control the temperature and the pressure, respectively. The thermostat and barostat time constants were 50 fs and 500 fs, respectively. The Lennard-Jones interactions were truncated at 1.2 nm and long-range tail corrections were applied for the energy and pressure calculation. The electrostatic interactions were calculated using the particle–particle particle–mesh (PPPM) method (Hockney and Eastwood, 1988) with a real space cutoff of 1.2 nm and a precision of 10^{-4} beyond the cutoff distance.

The equilibration of the system was started with a conjugate gradient energy minimization (Polak and Ribiere, 1969) for the initial configuration. Then a “simulated annealing process” (Kirkpatrick et al., 1983) was performed to avoid the trapping of the molecular structure in conformations that represent local minima. In the annealing process, the system was first heated to 490 K at $p = 0.1$ MPa and then slowly cooled to each target temperature at constant volume (NVT). When a target temperature was reached, another 10 ns NVT run was carried out to fully relax the system.

Then the system was simulated with a barostat (NPT) at the chosen p to find the appropriate density for 25 ns in which the averaged density was calculated over the last 5 ns. Longer equilibration times were used for elevated pressures. In the course of the equilibration, properties like temperature and pressure, as well as kinetic and potential energy, were monitored to ensure they reached steady state. The final configuration from the NPT equilibration run was resized to match the averaged density, followed by another NVT run for 20 ns. The resulting configuration served as the initial configuration for later NEMD or EMD simulations for the viscosity calculation.

In NEMD simulation, the system was sheared at fixed density and shear rate $\dot{\gamma}$ using the SLLOD equations of motion (Evans and Morriss, 2008). The stress tensor and other relevant state variables were monitored to determine if and when the steady state was reached. These variables were averaged and output every 10^5 time steps (i.e., 50 ps). The steady states were reached in a time of approximately $\dot{\gamma}^{-1}$ for all studied state points. After reaching steady state, the simulation was run for another 25 ns (40 ns for $p > 500$ MPa) and the shear stress was averaged over the last 20 ns (30 ns for $p > 500$ MPa) to obtain $\langle P_{xy} \rangle$ and compute the shear viscosity $\eta(\dot{\gamma})$ using Eq. (6). Block averaging and autocorrelation analysis (Grossfield et al., 2019) were performed for each production trajectory to assess the sampling quality and to calculate the uncertainty. Longer production length gave equivalent results on the scale of the symbol size in our plots. The procedure was repeated for various $\dot{\gamma}$ to obtain a spectrum of $\eta(\dot{\gamma})$ that covers Newtonian and non-Newtonian regimes. The range of $\dot{\gamma}$ varies with the temperature due to the shift of $\dot{\gamma}_c$. The simulated $\dot{\gamma}$ extends from 10^7 s^{-1} to 10^{10} s^{-1} , and no heating or other nonequilibrium effects were observed in this range. The obtained $\eta(\dot{\gamma})$ as a function of $\dot{\gamma}$ was then fit to the Eyring model or Carreau model to calculate η_N . The regression was performed with weights $\omega_i = 1/u_i^2$ (u_i is the expanded uncertainty of $\eta(\dot{\gamma}_i)$) using the Levenberg-Marquardt algorithm (Press et al., 1988). The weights were used to cancel out different degrees of noise at different $\dot{\gamma}$ and to propagate the uncertainty of $\eta(\dot{\gamma})$ to η_N . More details on the computing uncertainty analysis are given in Section 3.5.

For EMD simulations (viscosity production runs), the pressure tensor components were recorded every 5 fs, and the integrals in Eq. (11) were computed to 2 ns (correlation length). Nine independent production runs of 25 ns were carried out for a given temperature. Each run was started from the same configuration but with a different random seed for the initial velocity assignment. The viscosity values of the nine trajectories were averaged to give the Newtonian viscosity and estimate the computing uncertainty.

The above simulation parameters such as system size, timestep, simulation length, cutoff distance, and time integration window,

were chosen through a trial-and-error optimization procedure to ensure that the results were free from size effects and excessive computational cost. These parameters were set at the most conservative conditions, even though the optimal settings vary with force fields and thermodynamic states. The strategy may lead to unnecessarily long simulations in some cases, but it provides a reproducible comparison between the tested models and methods.

The code and data files for the simulations in this work have been made publicly available at https://github.com/LL8848/viscosity_md.

3.5. Computational uncertainties

In molecular dynamics simulation, macroscopic properties, like density and viscosity, are essentially random quantities, rather than deterministic, that should be reported with uncertainties because they are derived from microscopic molecular/atomistic trajectories using statistical mechanics. The quantities taken from molecular simulations are reported in the forms of two-sided confidence intervals: $\bar{x} \pm u$, where \bar{x} is the arithmetic mean of the quantity at equilibrium or steady state and u is the size of the confidence interval (aka expanded uncertainty). The expanded uncertainty is defined by $u = ks(\bar{x})$, where k is the coverage factor for 95% confidence level and $s(\bar{x})$ is the standard uncertainty. The block averaging method was used to estimate $s(\bar{x})$: first divide the production dataset of the quantity x into n blocks of equal lengths and calculate the average of each block; then calculate the standard deviation of the block averages $s(x_b)$, which yields a standard uncertainty of $s(\bar{x}) = s(x_b)/\sqrt{n}$. The block was set sufficiently long such that $s(\bar{x})$ was invariant of the block length. The autocorrelation function of x was calculated to check the “decorrelation” of the block averages and assist the selection of block length. The above protocol was used to estimate the uncertainties of ρ and $\eta(\dot{\gamma})$. The expanded uncertainties of $\eta(\dot{\gamma})$ were treated as weights in the fit that determines η_N . As η_N is one of the parameters of the fit function, its standard uncertainty can be readily calculated from the fit (with weights considered). The coverage factor for η_N was based on the number of varied $\eta(\dot{\gamma})$ used for fitting. Additional details on uncertainty quantification methods are provided in Ref. Grossfield et al. (2019).

4. Experimental results

Table 1 summarizes the measured density, dynamic viscosity, and kinematic viscosity of the lubricant PEC6 for temperatures from 258.15 K to 373.15 K and ambient pressure of 100.84 kPa. The values in Table 1 are the averages of three independent measurements at the same temperature. The measurements at the same temperatures are reproduced to within $\pm 0.2\%$ for most of the data. The raw data for all measurements can be found in the online repository linked to this paper (Lin and Kedzierski, 2020).

Fig. 3 plots the measured density as a function of temperature for all 72 data points. The solid line is the best-fit regression (or estimated mean) of the data to the following equation:

$$(\rho/\rho_0)^{-1} = A_0 + A_1 T_r \quad (13)$$

where ρ_0 is a reference density ($1000 \text{ kg}\cdot\text{m}^{-3}$) and T_r is the normalized temperature (i.e., $T_r = T/(273.15 \text{ K})$). The fitting constants are $A_0 = 0.766211$, $A_1 = 0.217297$. In Fig. 3, the lower and upper 95% simultaneous confidence intervals are drawn to either side of the mean, though they are difficult to see because they nearly coincide with the mean values. The residual standard deviation of the fit is $0.51 \text{ kg}\cdot\text{m}^{-3}$, which is 0.05% of the mean. The measurements in Ref. Fedele et al. (2007) are also shown in Fig. 3 (blue squares) for comparison, which are 0.5% lower than our density measurements. Although their measurements were done at slightly higher

Table 1

Measured density, dynamic viscosity, and kinematic viscosity of PEC6 at ambient pressure 100.84 kPa. Each value is the average of three independent measurements.

Temperature [K]	Density [$\text{kg}\cdot\text{m}^{-3}$]	Dynamic viscosity [mPa·s]	Kinematic viscosity [cSt]
258.15	1028.1	410.6	399.3
263.15	1024.3	275.7	269.1
268.15	1020.4	191.3	187.4
273.15	1016.5	136.3	134.1
278.15	1012.6	99.6	98.3
283.15	1008.7	74.4	73.8
288.15	1004.8	56.8	56.6
293.15	1000.9	44.3	44.3
298.15	997.0	35.1	35.2
303.15	993.2	28.2	28.4
308.15	989.3	23.0	23.3
313.15	985.4	19.1	19.4
318.15	981.5	16.0	16.3
323.15	977.7	13.5	13.8
328.15	973.9	11.6	11.9
333.15	970.0	10.0	10.3
338.15	966.2	8.7	9.0
343.15	962.4	7.6	7.9
348.15	958.7	6.7	7.0
353.15	954.9	6.0	6.2
358.15	951.1	5.3	5.6
363.15	947.3	4.8	5.1
368.15	943.6	4.3	4.6
373.15	939.9	3.9	4.2

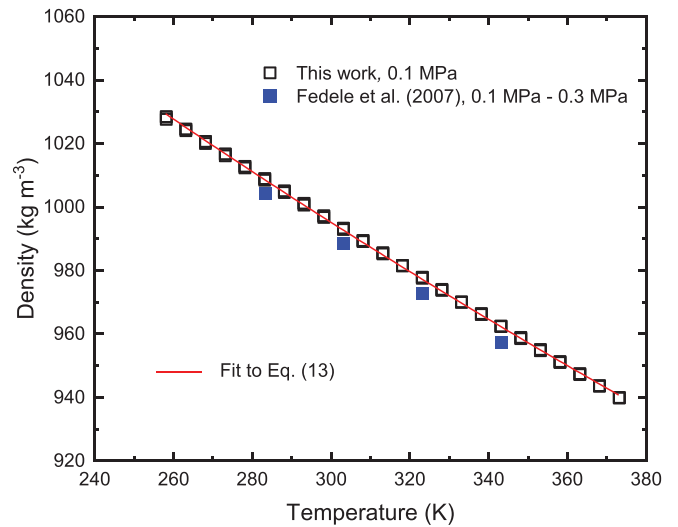


Fig. 3. Density measurements of PEC6. (For interpretation of the references to colour in this figure legend, the reader is referred to the web version of this article.)

pressure (i.e., 0.1 MPa to 0.3 MPa), the influence of this pressure difference on density is negligible according to the pressure-density relation measured by Fedele et al. (2007). The slight deviation could probably be attributed to the purity difference of the samples.

Fig. 4(a) plots the measured dynamic viscosity as a function of temperature for all 72 data points. The data are fit to the Vogel-Fulcher-Tammann (VFT) model:

$$\log \eta_N = A + \frac{B}{T - T_0} \quad (14)$$

with $A = -1.4007$, $B = 444.00144$, and $T_0 = 147.5425$. The residual standard deviation of the fit is $0.28 \text{ kg}\cdot\text{m}^{-3}$ (0.44% of the mean). The lower and upper 95% simultaneous confidence intervals are drawn but difficult to distinguish from the mean values. Our vis-

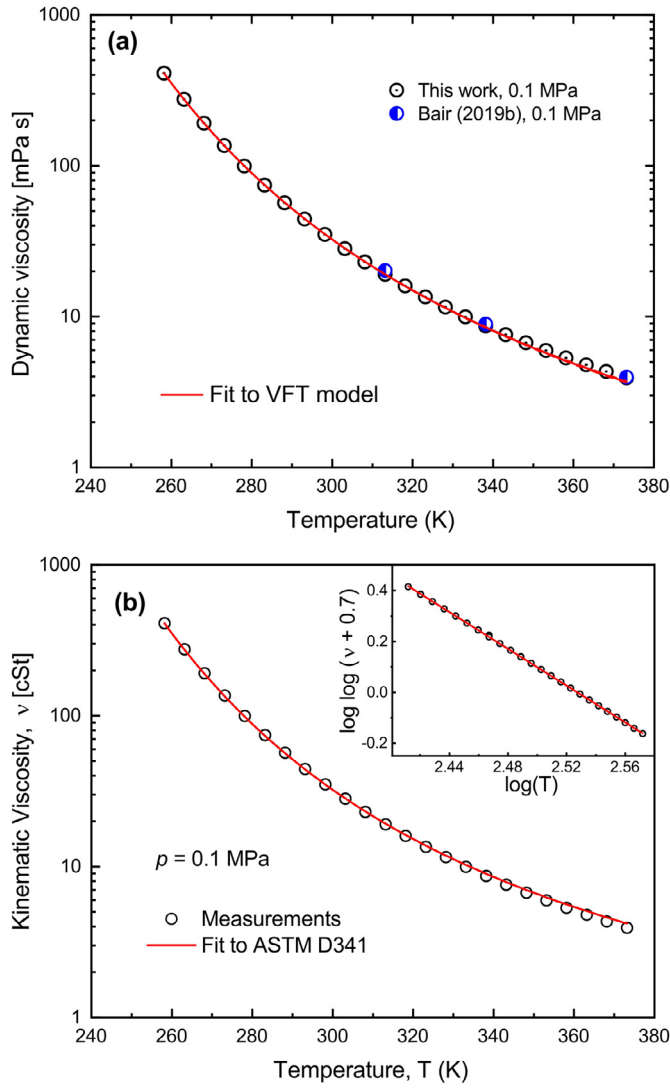


Fig. 4. Viscosity measurements of PEC6: (a) dynamic viscosity; (b) kinematic viscosity.

cosity measurements agree well with those in Ref. (Bair, 2019b) (i.e., within uncertainty). Fig. 4(b) shows the kinematic viscosity calculated from the measured density and dynamic viscosity. The kinematic viscosity data are fit to the correlation used in the standard ASTM D341-20, 2020:

$$\log(\log(\nu + 0.7)) = A - B \log T \quad (15)$$

with $A = 9.13581$ and $B = 3.61484$. The insert of Fig. 4(b) shows good linearity between $\log(\log(\nu + 0.7))$ and $\log T$ in the test temperature range (258.15 K to 373.15 K).

5. Simulation results

5.1. MD prediction for density

Fig. 5 shows the computed densities using force fields of OPLS, LOPLS, and DREIDING along with selected experimental data. The error bars are not easily visible because the uncertainties are approximately the symbol size. The dashed lines are best-fit regressions of the data to Eq. (13). As shown in Fig. 5, the density prediction of OPLS is in excellent agreement with the measurements, i.e., within $\pm 0.2\%$ of the measurement for temperatures 258 K to 373 K. LOPLS also yields rather accurate density prediction at

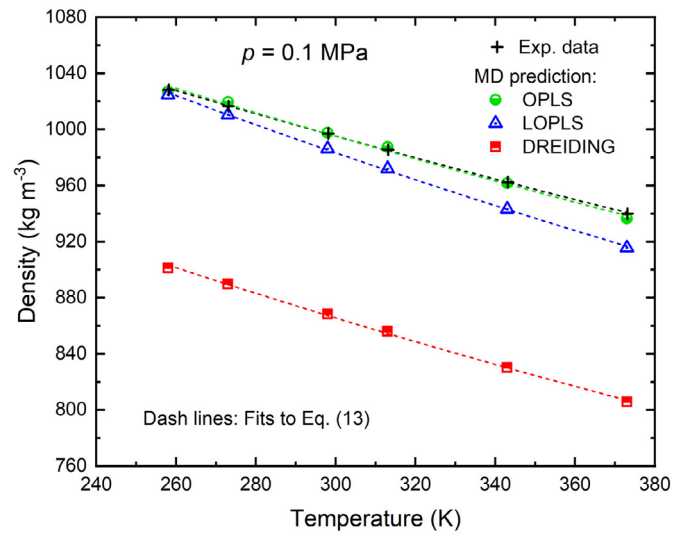


Fig. 5. MD density prediction for PEC6 using different force fields.

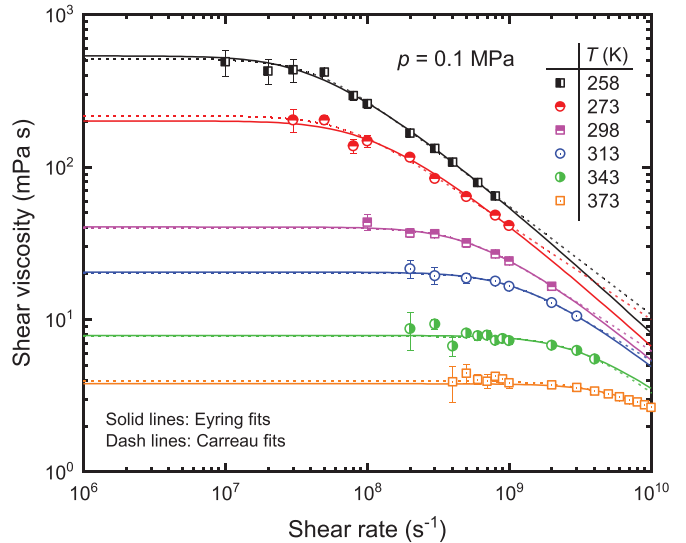


Fig. 6. Shear dependence of viscosity for different temperatures. Computed by NEMD using LOPLS force field.

258 K (4.9 kg·m⁻³ or 0.5% smaller than the measurement), but the density drifts slightly with increasing temperature. At 373 K, the deviation between the predicted density by LOPLS and the measurement increases to 25.2 kg·m⁻³ (2.7% of the measurement). On average, LOPLS underestimates the density by 1.4%. The generic force field DREIDING significantly underestimates the density with an offset of approximately 130 kg·m⁻³ (13% of the measurement mean).

5.2. MD prediction for viscosity

5.2.1. Shear and temperature dependences of viscosity at ambient pressure

Fig. 6 shows the shear viscosities computed from NEMD simulations as a function of shear rate ($\dot{\gamma}$) for different temperatures (258 K to 373 K, 0.1 MPa). Only the simulations using the LOPLS force field are shown here because it provides the most realistic viscosity prediction (see Fig. 7 which will be discussed later). The error bars to either side of the symbols represent the degree to which the viscosity fluctuates in the course of NEMD simulations. The fluctuation of viscosity is mainly caused by the thermal motion

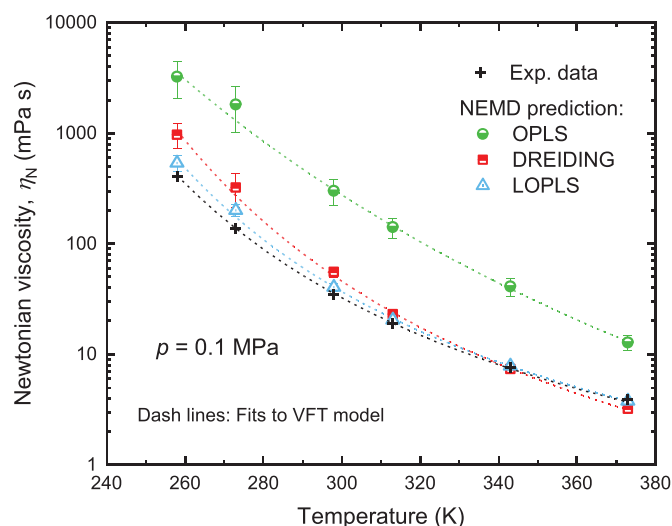


Fig. 7. Temperature dependence of Newtonian viscosity predicted by NEMD using different force fields.

of molecules, or “thermal noise”. The atomistic positions continuously fluctuate as a result of thermal motion, leading to the fluctuation of the system’s momenta and total potential energy, which both contribute to the stress tensor \mathbf{P} (see Eq. (7)), and consequently cause the viscosity to fluctuate ($\eta = P_{xy} / \dot{\gamma}$). As shown in Fig. 6, the fluctuation of viscosity intensifies as the shear rate decreases. This is because the shear stress decreases with decreasing shear rate while the thermal noise remains unchanged, resulting in a decrease of signal-to-noise ratio. At low shear rates where fluctuations are significant, the response of the lubricant molecules to the shear perturbation is relatively weak compared to the thermal motion. Note that the thermal motion is temperature dependent, thus the errors are relatively larger at higher temperatures for the same shear rate.

As shown in Fig. 6, the viscosity of PEC6 plateaus at low shear rate (i.e., Newtonian regime) and decreases with increasing shear rate at high shear rate (i.e., shear thinning). The critical shear rate $\dot{\gamma}_c$ at which the lubricant transitions from Newtonian regime to shear-thinning is higher at higher temperature. The increased $\dot{\gamma}_c$ with increasing temperature can be explained by the mechanism of shear induced molecular alignment (Cui et al., 1998b; Davis and Evans, 1994). Under low shear rates, the shear imposed on molecules can be balanced out by the molecular relaxation. When the shear rate exceeds a critical value, which is approximately the inverse of the longest relaxation time, molecules cannot respond fast enough to the shear deformation as caused by the flow field, and consequently tend to align with the flow field to relieve the stress. The molecular alignment leads to a reduced viscosity of the lubricant, i.e., shear thinning. At higher temperature, the molecules move and rotate more quickly, resulting in a shorter relaxation time and therefore a higher $\dot{\gamma}_c$.

The solid and dash lines in Fig. 6 are the best-fit regressions of the NEMD-computed shear viscosities $\eta(\dot{\gamma})$ to the Eyring model (Eq. (9)) and the Carreau model (Eq. (10)), respectively. The fitting parameters and metrics are listed in Table 2. It can be seen that the shear viscosities are equally well fit by both models for the range of simulated shear rates. The extrapolations of the fits to low shear rates, which equal to the Newtonian viscosity, are also very close. The Carreau fit only deviates from the Eyring fit at high shear rates, for example, $\dot{\gamma} > 10^9 \text{ s}^{-1}$ for the curves of 258 K and 273 K. Considering that the Eyring model has only two fitting parameters while the Carreau has an extra parameter (n), and that the Eyring outperforms the Carreau for large viscosity

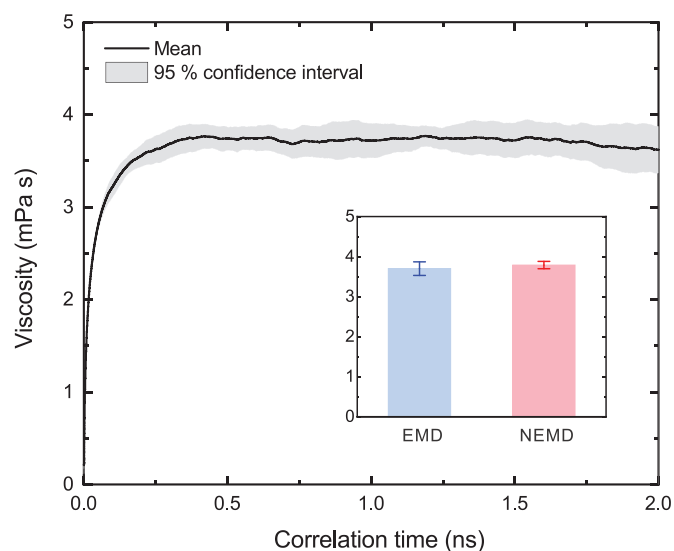


Fig. 8. Viscosity computed by EMD simulations, averaged from nine independent EMD trajectories. The inset shows the η_N calculated by EMD and NEMD. Force field: LOPLS.

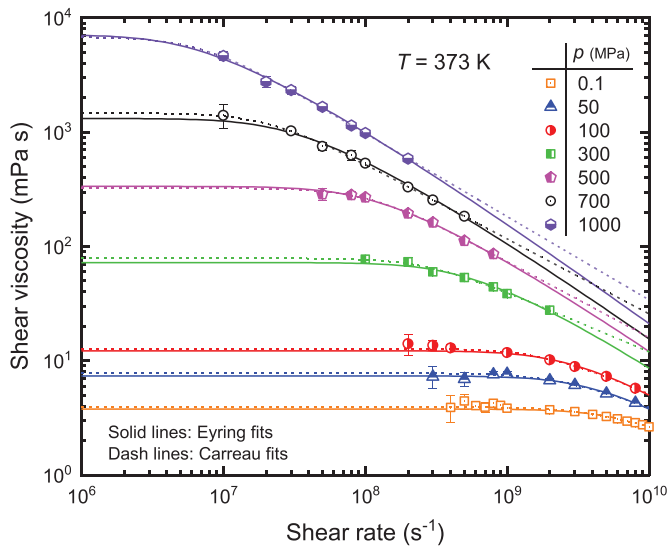
(Jadhao and Robbins, 2019), the Eyring model was primarily used to fit $\eta(\dot{\gamma})$ and calculate η_N in this study. More details on the comparison between Eyring and Carreau models are given in Section 5.2.3.

Fig. 7 shows the Newtonian viscosity η_N as a function of temperature obtained from Eyring fits. The results for force fields of LOPLS, OPLS, and DREIDING are given, along with selected experimental data. The dash lines in Fig. 7 are the best-fit regressions of η_N to the VFT model (Eq. (14)). The deviation between the LOPLS-predicted η_N and the measurement is between 3% and 47% for 258 K to 373 K. The relatively large deviation at low temperature is partly due to the increased uncertainties of η_{NEMD} and η_N with decreasing temperature. Despite the excellent accuracy of the density prediction, OPLS dramatically overpredicts η_N by 200% to 1000%. Similar large viscosity obtained by OPLS was observed by Siu et al. (2012) for dodecane and pentadecane, who attributed it to the gel-like phase transition misled by OPLS parameters. Surprisingly, even though DREIDING underpredicts the density by a considerable offset, its η_N prediction agrees well (i.e., within $\pm 20\%$) with the measurement for $T \geq 313 \text{ K}$. The DREIDING-predicted η_N starts to deviate from the measured value significantly when temperature goes below 313 K. At 258 K, the DREIDING overpredicts η_N by 140%. Similarly, Ewen et al. (2016) also observed that DREIDING had poor prediction accuracy for the density of long-chain alkanes but relatively good for the viscosity.

EMD simulations were also carried out to verify the NEMD simulation results. Fig. 8 shows the viscosity computed by Eq. (11) from EMD simulations for 373 K and 0.1 MPa. The solid line is the mean of nine independent EMD trajectories, and the shaded areas to either side of the mean curve represent the 95% confidence intervals, which are calculated by ks/\sqrt{n} where k is the coverage factor, s is the standard deviation, and $n = 9$. As shown in Fig. 8, the viscosity reaches a plateau at the correlation time of approximately 0.5 ns. The Newtonian viscosity can be estimated from the plateau value, $3.7 \pm 0.2 \text{ mPa}\cdot\text{s}$, which reasonably verifies the one calculated with the NEMD simulations ($3.8 \pm 0.1 \text{ mPa}\cdot\text{s}$). The increase in error with respect to correlation time in the EMD simulation is due to the accumulation of thermal noise at long times in the correlation function (Zhang et al., 2015). For temperatures below 373 K, the viscosity increases exponentially, and longer correlation lengths are needed for EMD simulation due to the increased

Table 2Parameters and errors of Eyring fits and Carreau fits for shear viscosities $\eta(\dot{\gamma}_i)$ that are computed from NEMD simulations using LOPLS force field.

State points		Eyring Fits						Carreau Fits					
T (K)	P (MPa)	η_N	τ	$\dot{\gamma}_c = \tau^{-1}$	w. RMSE ^a	η_N error (%) ^b		η_N	τ	n	$\dot{\gamma}_c = \tau^{-1}$	w. RMSE ^a	η_N error (%) ^b
258	0.1	536.6	4.5E-08	2.2E+07	0.8	30.7		514.1	2.3E-08	0.29	4.4E+07	0.7	25.2
273	0.1	200.9	1.8E-08	5.7E+07	1.3	47.4		217.3	1.4E-08	0.38	7.0E+07	1.2	59.4
298	0.1	40.5	3.1E-09	3.2E+08	0.4	15.4		40.0	2.0E-09	0.38	4.9E+08	0.5	14.0
313	0.1	20.5	1.4E-09	7.2E+08	0.4	7.3		20.3	9.7E-10	0.42	1.0E+09	0.4	6.5
343	0.1	7.9	5.3E-10	1.9E+09	1.1	3.5		7.8	4.2E-10	0.49	2.4E+09	1.1	2.3
373	0.1	3.8	2.2E-10	4.5E+09	0.8	−3.5		3.9	2.7E-10	0.62	3.7E+09	0.6	0.4
373	50	7.4	4.1E-10	2.4E+09	0.9	2.9		7.8	4.6E-10	0.56	2.2E+09	0.5	8.6
373	100	12.2	6.2E-10	1.6E+09	0.8	9.0		12.8	5.8E-10	0.49	1.7E+09	0.6	14.2
373	300	72.3	3.6E-09	2.8E+08	1.2	43.5		79.1	3.7E-09	0.48	2.7E+08	0.7	57.0
373	500	335.5	1.6E-08	6.2E+07	0.7	n/a		323.7	9.2E-09	0.33	1.1E+08	0.7	n/a
373	700	1318.4	6.0E-08	1.7E+07	0.8	n/a		1472.2	4.8E-08	0.34	2.1E+07	0.4	n/a
373	1000	7127.6	2.9E-07	3.4E+06	0.6	n/a		6827.0	1.4E-07	0.27	7.0E+06	0.5	n/a

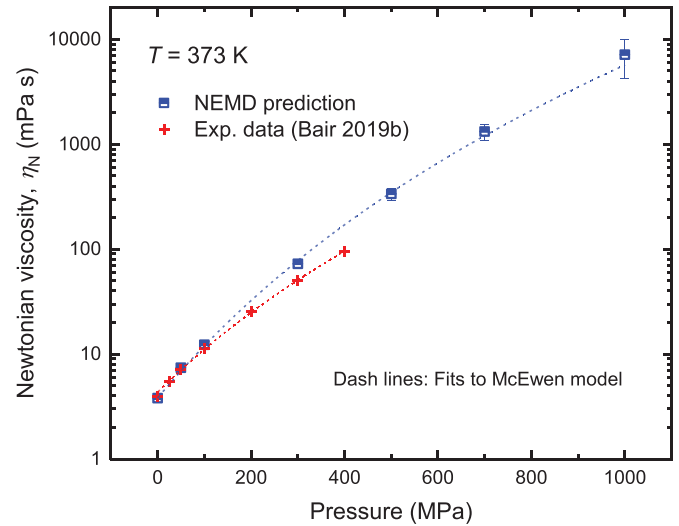
^a Root-mean-squared error weighted by $\omega_i = 1/u_i^2$ (u_i is the expanded uncertainty of $\eta(\dot{\gamma}_i)$).^b Prediction error of Newtonian viscosity: $(\eta_{N,fit} - \eta_{N,exp})/\eta_{N,exp}$.**Fig. 9.** Shear dependence of viscosity for different pressures. Computed by NEMD using LOPLS force field.

relaxation time, which will dramatically increase the CPU time. The CPU time for NEMD is relatively less sensitive to the simulation temperature. As such, NEMD is more efficient in the computation of viscosity for relatively large molecules such as polyol esters over a wide range of temperatures.

5.2.2. Pressure dependence of viscosity

Fig. 9 shows shear viscosities computed by NEMD using LOPLS force field for pressures up to 1 GPa. The temperature is fixed at 373 K. The shear viscosity η_{NEMD} are fit to both Eyring model and the Carreau model, as shown in solid lines and dash lines in Fig. 9, respectively. The parameters for the fittings are given in Table 2. Similarly, the η_{NEMD} are equally well fit by both models for the range of simulated shear rates. As shown in Fig. 9, the critical shear rate $\dot{\gamma}_c$ (i.e., the onset of shear-thinning) decreases with increasing pressure. With the pressure increased from 0.1 MPa to 1 GPa, $\dot{\gamma}_c$ decreases from $4.5 \times 10^9 \text{ s}^{-1}$ to $3.4 \times 10^6 \text{ s}^{-1}$ as estimated by the Eyring fits.

Fig. 10 shows the Newtonian viscosity η_N as a function of pressure obtained from Eyring fits. The prediction is compared with the experimental data from Ref. Bair (2019b). The η_N for lower pressures ($\leq 100 \text{ MPa}$) match the experimental data very well (within $\pm 10\%$), whereas they start to diverge at 300 MPa. However, the less-than-exponential rising trend of η_N with respect to

**Fig. 10.** Pressure dependence of Newtonian viscosity predicted by NEMD using LOPLS force field.

pressure, as exhibited by the experimental data, is reproduced by the prediction. The data as well as the predictions are therefore fit to the McEwen model which is widely used to model less-than-exponential pressure–viscosity response (Bair, 2019c):

$$\eta_N = \eta_0 \left(1 + \frac{\alpha_0}{q} p \right)^q \quad (16)$$

where $\eta_0 = 4.3385$, $\alpha_0 = 0.0102$ and $q = 5.8433$ for the experimental data and $\eta_0 = 3.8225$, $\alpha_0 = 0.0124$ and $q = 7.4961$ for the predictions. Note that the McEwen fit slightly diverges from the predicted η_N at 1 GPa, indicating that there may be a transition of pressure–viscosity response from less-than-exponential to exponential at between 800 MPa and 1000 MPa.

5.2.3. Eyring fit vs Carreau fit

Table 2 lists the fitting parameters and metrics of Eyring fits and Carreau fits for all the state points simulated using LOPLS. The parameters η_N and τ of Eyring fits and Carreau fits are rather close, and both η_N are within similar errors with the measurements. The RMSE (root-mean-squared error, also called residual standard deviation) of the fit is weighted by $\omega_i = 1/u_i^2$ where u_i is the expanded uncertainty of $\eta(\dot{\gamma}_i)$, in accordance with the regression process of the fits. A weighted RMSE = 1 means the residuals of the fits are comparable to the uncertainty of the input data (i.e., $\eta(\dot{\gamma}_i)$, computed from NEMD simulations). As can be seen from Table 2, the

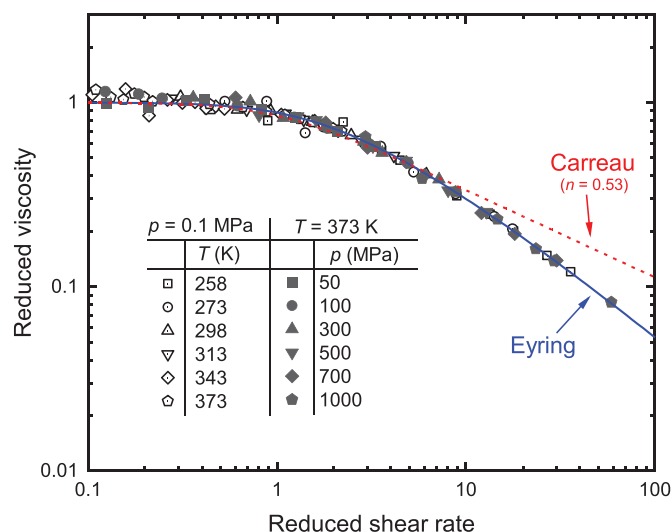


Fig. 11. Reduced viscosity (η/η_N) as a function of reduced strain rate ($\dot{\gamma}/\dot{\gamma}_c$) for all data computed by NEMD using the LOPLS force field.

weighted RMSE of Eyring fits and Carreau fits are also close and mostly less than 1. From the perspective of fitting statistics, therefore, the viscosity of PEC6 is equally well described by Eyring and Carreau models for the states simulated herein ($\eta_N < 10^4$ mPa·s). As such, Eyring model will be preferred due to less parameter required.

Fig. 11 further demonstrates the success of Eyring model in describing the viscosity of PEC6. The reduced viscosity (η/η_N) is plotted against reduced shear rate ($\dot{\gamma}/\dot{\gamma}_c$) for all NEMD simulations (using LOPLS force field) over a wide range of temperature and pressure. As shown in Fig. 11, all reduced data fall on a universal curve of the analytic solution of the Eyring model. The excellent collapse indicates that the rheological response of PEC6 obeys the time–temperature–pressure superposition hypothesis that assumes a shear viscosity curve (η vs $\dot{\gamma}$) can be superimposed over another curve for different temperature or pressure by shifting the curve and scaling the associated relaxation time. Our results show that the collapse of the viscosity of PEC6 to the Eyring equation applies to η_N from approximately 1 mPa·s to 10^4 mPa·s. We expect that the Eyring equation will also apply to higher viscosity, considering that the variation of energy barrier tends to diminish as η_N increases, which accords better with the assumption of single energy barrier in Eyring theory (Jadhao and Robbins, 2017). Fig. 11 also plots the Carreau equation with a constant power exponent $n = 0.53$ that is obtained by regressing all reduced data. The Carreau equation with $n = 0.53$ fits well for low reduced rates but significantly diverges from the data (and Eyring equation) for reduced rate higher than 10. Hence, no universal Carreau equation can describe all viscosity of PEC6. This is also evident from Table 2 where the best-fit n of Carreau fits for different state points are varied appreciably with temperature and pressure.

6. Discussion

The above results show that density and viscosity can be obtained at a remarkably broad range of temperature and pressure by MD simulations. The viscosity at giga-pascal, which is difficult to measure experimentally, can be readily computed from a few simulations with quantified uncertainty. The pressure–viscosity coefficient as well as the temperature–viscosity coefficient can also be derived based on different definitions (Bair, 2000). All these properties are crucial to determine the film thickness in concentrated contacts where pressure often exceeds 0.5 GPa.

The only input for the above predictions, in addition to state conditions (T , p , etc.), is the molecular topology (or chemical structure) of PEC6. Note that PEC6 or similar polyol ester molecules (for example, pentaerythritol tetraesters) are not used for the parametrization of any of studied force fields (OPLS, LOPLS, DREIDING). In addition, the parameters of these force fields are generally optimized for density and heat of vaporization, without explicit consideration of viscosity and other transport properties. Therefore, our prediction based on MD simulations is *pure prediction*.

In particular, LOPLS shows relatively good prediction accuracy for viscosity and density, which implies a good transferability of the LOPLS force field in polyol esters, meaning that it can be applied to model other POE lubricants and perhaps other classes of lubricants. The systematic deviation between prediction and experimental data indicates that the prediction accuracy could be improved by further refining the force field parameters. Despite the deviation of absolute values, the NEMD simulation accurately captured the trend with respect to temperature and pressure. In practice, trends in properties are as valuable as the quantitative accuracy in property predictions.

7. Conclusions

In this study, molecular dynamics (MD) is shown to be a reliable method to predict the density and the viscosity of POE lubricants over a very wide range of temperature and pressure. The density can be readily obtained with high accuracy from standard MD simulations. The viscosity, on the other hand, can be obtained from the nonequilibrium molecular dynamics simulations (NEMD) in combination with Eyring fits. The NEMD simulation adequately simulates the viscosity response to shear at different temperature and pressure, and the Eyring model well describes the correlation between viscosity and shear rate. The simulated density and viscosity as well as their dependencies with temperature and pressure can be employed to predict film thickness of lubricants.

Detailed simulation results of lubricant PEC6 are presented for temperatures from 258 K to 373 K and pressures from 0.1 MPa to 1 GPa. The predictions are compared with new experimental data of PEC6 for 258 K to 373 K at ambient pressure as well as high-pressure data from the literature. The accuracy of a MD simulation is highly reliant on the selected force field. Overall, LOPLS is the most accurate force field for PEC6. It predicts the density of PEC6 to within $\pm 3\%$, and Newtonian viscosity η_N to within 50% for η_N up to 1 Pa·s. The LOPLS force field and the computation techniques herein are expected to apply to other polyol esters and perhaps other classes of lubricants.

Acknowledgement

This work was funded by the National Institute of Standards and Technology (NIST), United States, under Project No. 7321107. Thanks go to the following NIST personnel for their constructive criticism of the draft manuscript: A. Pertzborn, M. Huber and G. Linteris. The computations were performed on the NIST High Performance Computing (HPC) Clusters. The chemical sample of pentaerythritol tetrahexanoate (PEC6) was synthesized and donated by Philip Chan of the Toronto Research Chemicals, Canada.

Declaration of Competing Interest

The authors declare that they have no known competing financial interests or personal relationships that could have appeared to influence the work reported in this paper.

Appendix A. : OPLS parameters²

Tables A1, A2, A3

Table A1

Non-bonded parameters.

Atom type	Description	q (e)	σ (nm)	ϵ (kJ·mol ⁻¹)
CT	alkane carbon (-CH ₃)	-0.18	0.350	0.276144
CT	alkane carbon (-CH ₂)	-0.12	0.350	0.276144
CT	alkane carbon (>C<)	0.00	0.350	0.276144
HC	alkane hydrogen (H-C)	0.06	0.250	0.125520
C_2	ester carbonyl carbon (-COOR)	0.51	0.375	0.439320
O_2	ester carbonyl oxygen (=O)	-0.43	0.296	0.878640
OS	alkoxy oxygen (CO-O-R)	-0.33	0.300	0.711280
HC	α -methoxy hydrogen (-OCH ₂ -)	0.03	0.242	0.062760
CT	alkoxy carbon (-OCH ₂ R)	0.19	0.350	0.276144

Table A2

Bond stretching and angle bending parameters.

Bond stretching			Angle bending		
Bond	r_0 (nm)	K_r (kJ·mol ⁻¹ ·nm ⁻²)	Angle	θ_0 (deg)	K_θ (kJ·mol ⁻¹ ·deg ⁻²)
C_2-O_2	0.1229	238488.0	CT-C_2-O_2	120.4	334.72
C_2-CT	0.1522	132632.8	OS-C_2-CT	111.4	338.90
OS-C_2	0.1327	89537.6	OS-C_2-O_2	123.4	347.27
CT-CT	0.1529	112131.2	CT-CT-CT	112.7	244.14
CT-OS	0.1410	133888.0	C_2-CT-CT	111.1	263.59
CT-HC	0.1090	142256.0	CT-CT-OS	109.5	209.20
			HC-CT-HC	107.8	138.07
			C_2-CT-HC	109.5	146.44
			OS-CT-HC	109.5	146.44
			CT-CT-HC	110.7	156.90
			CT-OS-C_2	116.9	347.27

Table A3

Torsional parameters.

Dihedral	V_1 (kJ·mol ⁻¹)	V_2 (kJ·mol ⁻¹)	V_3 (kJ·mol ⁻¹)
CT-CT-C_2-O_2	-1.158968	5.137952	-2.903696
O_2-C_2-CT-HC	0.000000	0.000000	0.000000
OS-C_2-CT-CT	0.000000	0.000000	-2.313752
OS-C_2-CT-HC	0.000000	0.000000	0.552288
CT-OS-C_2-O_2	0.000000	21.438816	0.000000
CT-OS-C_2-CT	19.535096	21.438816	0.000000
C_2-CT-CT-CT	-7.100248	-1.907904	2.447640
C_2-CT-CT-HC	0.000000	0.000000	-0.317984
CT-CT-CT-CT	5.439200	-0.209200	0.836800
CT-CT-CT-HC	0.000000	0.000000	1.255200
HC-CT-CT-HC	0.000000	0.000000	1.255200
CT-CT-OS-C_2	-5.104480	-0.527184	1.765648
C_2-OS-CT-HC	0.000000	0.000000	0.828432
CT-CT-CT-OS	7.158824	-2.092000	2.773992
Improper dihedral	K_χ (kJ·mol ⁻¹)	χ_0 (deg)	
OS-(C_2=O_2)-CT	43.932	180	

² Taken from the literature (Jorgensen et al., 1996; Robertson et al., 2015). Conversions for unit or functional form may apply.

Appendix B. LOPLS parameters³

Tables B1, B2

Table B1

Non-bonded parameters.

Atom type	Description	q (e)	σ (nm)	ϵ (kJ·mol ⁻¹)
CT	alkane carbon (CH ₃ -)	-0.222	0.350	0.276144
CT	alkane carbon (-CH ₂)	-0.148	0.350	0.276144
CT	alkane carbon (>C<)	0.000	0.350	0.276144
HC	alkane hydrogen (H-CH ₃)	0.074	0.250	0.125520
HC	alkane hydrogen (H-CH ₂)	0.074	0.250	0.110000
C_2	ester carbonyl carbon (-COOR)	0.750	0.319	0.439320
O_2	ester carbonyl oxygen (=O)	-0.550	0.311	0.702912
OS	alkoxy oxygen (CO-O-R)	-0.450	0.255	0.711280
HC	alpha-methoxy hydrogen (-OCH<)	0.030	0.242	0.062760
CT	alkoxy carbon (-OCH ₂ R)	0.190	0.350	0.276144

Bond stretching and angle bending parameters of LOPLS are the same as those of OPLS.

Table B2

Torsional parameters.

Dihedral	V_1 (kJ·mol ⁻¹)	V_2 (kJ·mol ⁻¹)	V_3 (kJ·mol ⁻¹)
CT-CT-C_2-O_2	-1.154865	5.174990	-2.806395
O_2-C_2-CT-HC	0.000000	0.000000	0.000000
OS-C_2-CT-CT	3.702790	-2.622970	-2.064150
OS-C_2-CT-HC	-0.031065	0.009110	0.467785
CT-OS-C_2-O_2	0.000000	24.006620	0.000000
CT-OS-C_2-CT	13.050860	24.006590	0.000000
C_2-CT-CT-CT	-9.654065	-2.624730	2.602245
C_2-CT-CT-HC	-0.008850	0.072610	-1.235150
CT-CT-CT-CT	2.697394	-0.896807	0.745670
CT-CT-CT-HC	0.000000	0.000000	1.255200
HC-CT-CT-HC	0.000000	0.000000	1.255200
CT-CT-OS-C_2	-7.260905	-5.223490	2.610385
C_2-OS-CT-HC	-0.000010	0.000000	0.828430
CT-CT-CT-OS	9.450460	-4.284770	4.213720
Improper dihedral	K_χ (kJ·mol ⁻¹)	χ_0 (deg)	
OS-(C_2=O_2)-CT	43.932	180	

Appendix C. : DREIDING parameters⁴

Tables C1, C2, C3

Table C1

Non-bonded parameters (Partial charges are assigned using the Gasteiger estimates (Gasteiger and Marsili, 1980)).

Atom type	Description	σ (nm)	ϵ (kJ·mol ⁻¹)
CT	alkane carbon	0.347	0.397480
OS	alkoxy oxygen	0.303	0.401664
O_2	alkoxy oxygen	0.303	0.401664
C_2	ester carbonyl carbon	0.347	0.397480
HC	alkane hydrogen	0.285	0.062760

³ Taken from the literature (Pluhackova et al., 2015; Siu et al., 2012). Conversions for unit or functional form may apply.

⁴ Taken from the literature (Mayo et al., 1990). Conversions for unit or functional form may apply.

Table C2
Bond stretching and angle bending parameters.

Bond stretching			Angle bending		
Bond	r_0 (nm)	K_r (kJ·mol ⁻¹ ·nm ⁻²)	Angle	θ_0 (deg)	K_θ (kJ·mol ⁻¹ ·deg ⁻²)
C_2–O_2	0.122	292,880	CT–C_2–O_2	120	209.2
C_2–CT	0.143	146,440	OS–C_2–CT	120	209.2
OS–C_2	0.132	146,440	OS–C_2–O_2	120	209.2
CT–CT	0.153	146,440	CT–CT–CT	109.47	209.2
CT–OS	0.142	146,440	C_2–CT–CT	109.47	209.2
CT–HC	0.109	146,440	CT–CT–OS	109.47	209.2
			HC–CT–HC	109.47	209.2
			C_2–CT–HC	109.47	209.2
			OS–CT–HC	109.47	209.2
			CT–CT–HC	109.47	209.2
			CT–OS–C_2	104.51	209.2

Table C3
Torsional parameters.

Dihedral	K_ϕ (kJ·mol ⁻¹)	d (-)	n (-)
CT–CT–C_2–O_2	0.348527	–1	6
O_2–C_2–CT–HC	0.348527	–1	6
OS–C_2–CT–CT	0.697473	1	3
OS–C_2–CT–HC	0.697473	1	3
CT–OS–C_2–O_2	2.092000	–1	2
CT–OS–C_2–CT	2.092000	–1	2
C_2–CT–CT–CT	0.464842	1	3
C_2–CT–CT–HC	0.464842	1	3
CT–CT–CT–CT	0.464842	1	3
CT–CT–CT–HC	0.464842	1	3
HC–CT–CT–HC	0.464842	1	3
CT–CT–OS–C_2	1.394527	1	3
C_2–OS–CT–HC	1.394527	1	3
CT–CT–CT–OS	0.464842	1	3
Improper dihedral	K_χ (kJ·mol ⁻¹)	χ_0 (deg)	
OS–(C_2=O_2)–CT	83.68	0	

References

- ASTM D341-20, 2020. *Standard Practice for Viscosity-Temperature Equations and Charts for Liquid Petroleum or Hydrocarbon Products*. ASTM International, West Conshohocken, PA.
- Bair, S., 2019a. An Introduction to Elastohydrodynamic Lubrication. In: *High Pressure Rheology for Quantitative Elastohydrodynamics*. Elsevier, pp. 1–19. doi:10.1016/B978-0-444-64156-4.00001-5.
- Bair, S., 2019b. The Pressure and Temperature Dependence of the Low-Shear Viscosity. In: *High Pressure Rheology for Quantitative Elastohydrodynamics*. Elsevier, pp. 97–133. doi:10.1016/B978-0-444-64156-4.00005-2.
- Bair, S., 2019c. Correlations for the Temperature and Pressure and Composition Dependence of Low-Shear Viscosity. In: *High Pressure Rheology for Quantitative Elastohydrodynamics*. Elsevier, pp. 135–182. doi:10.1016/B978-0-444-64156-4.00006-4.
- Bair, S., 2000. Pressure-viscosity behavior of lubricants to 1.4 gpa and its relation to ehd traction. *Tribol. Trans.* 43, 91–99. doi:10.1080/10402000008982317.
- Bobbo, S., Pernechele, F., Fedele, L., Stryjek, R., 2008. Solubility measurements and data correlation of carbon dioxide in pentaerythritol tetrahexanoate (PEC6). *J. Chem. Eng. Data* 53, 2581–2585. doi:10.1021/je800429j.
- Carreau, P.J., 1972. Rheological equations from molecular network theories. *Trans. Soc. Rheol.* 16, 99–127. doi:10.1122/1.549276.
- Chen, T., Smit, B., Bell, A.T., 2009. Are pressure fluctuation-based equilibrium methods really worse than nonequilibrium methods for calculating viscosities? *J. Chem. Phys.* 131, 246101. doi:10.1063/1.3274802.
- Cui, S.T., Cummings, P.T., Cochran, H.D., 1998a. The calculation of viscosity of liquid n-decane and n-hexadecane by the Green-Kubo method. *Mol. Phys.* 93, 117–122. doi:10.1080/002689798169500.
- Cui, S.T., Cummings, P.T., Cochran, H.D., Moore, J.D., Gupta, S.A., 1998b. Nonequilibrium molecular dynamics simulation of the rheology of linear and branched alkanes. *Int. J. Thermophys.* 19, 449–459. doi:10.1023/A:1022565427881.
- Daivis, P.J., Evans, D.J., 1994. Comparison of constant pressure and constant volume nonequilibrium simulations of sheared model decane. *J. Chem. Phys.* 100, 541–547. doi:10.1063/1.466970.
- Evans, D.J., Morriss, G., 2008. *Statistical mechanics of nonequilibrium liquids*. Statistical Mechanics of Nonequilibrium Liquids, 2nd ed. doi:10.1017/CBO9780511535307.
- Ewell, R.H., Eyring, H., 1937. Theory of the viscosity of liquids as a function of temperature and pressure. *J. Chem. Phys.* 5, 726–736. doi:10.1063/1.1750108.
- Ewen, J.P., Gattinoni, C., Thakkar, F.M., Morgan, N., Spikes, H.A., Dini, D., 2016. A comparison of classical force-fields for molecular dynamics simulations of lubricants. *Materials (Basel)* 9, 1–17. doi:10.3390/ma9080651.
- Eyring, H., 1936. Viscosity, plasticity, and diffusion as examples of absolute reaction rates. *J. Chem. Phys.* 4, 283–291. doi:10.1063/1.1749836.
- Fedele, L., Marinetti, S., Bobbo, S., Scattolini, M., 2007. PpT experimental measurements and data correlation of pentaerythritol esters. *J. Chem. Eng. Data* 52, 108–115. doi:10.1021/je060271a.
- Frenkel, D., Smit, B. (Eds.), 2002. Appendix C - Linear Response Theory. In: *Understanding Molecular Simulation*, 2nd ed. Academic Press, San Diego, pp. 509–523. doi:10.1016/B978-012267351-1/50022-5.
- Gasteiger, J., Marsili, M., 1980. Iterative partial equalization of orbital electronegativity—a rapid access to atomic charges. *Tetrahedron* 36, 3219–3228. doi:10.1016/0040-4020(80)80168-2.
- Grossfield, A., Patrone, P.N., Roe, D.R., Schult, A.J., Siderius, D., Zuckerman, D.M., 2019. Best practices for quantification of uncertainty and sampling quality in molecular simulations [Article v1.0]. *Living J. Comput. Mol. Sci.* 1, 1–24. doi:10.33011/livecoms.1.1.5067.
- Hess, B., 2002. Determining the shear viscosity of model liquids from molecular dynamics simulations. *J. Chem. Phys.* 116, 209–217. doi:10.1063/1.1421362.
- Hockney, R.W., Eastwood, J.W., 1988. *Computer Simulation Using Particles*. IOP Publishing Ltd. doi:10.1887/0852743920.
- Hoover, W.G., 1985. Canonical dynamics: equilibrium phase-space distributions. *Phys. Rev. A* 31, 1695–1697. doi:10.1103/PhysRevA.31.1695.
- Jadhao, V., Robbins, M.O., 2019. Rheological properties of liquids under conditions of elastohydrodynamic lubrication. *Tribol. Lett.* 67, 1–20. doi:10.1007/s12429-019-1178-3.
- Jadhao, V., Robbins, M.O., 2017. Probing large viscosities in glass-formers with nonequilibrium simulations. *Proc. Natl. Acad. Sci.* 114, 7952–7957. doi:10.1073/pnas.1705978114.
- Jewett, A., 2019. Moltemplate. <https://www.moltemplate.org/>.
- Jorgensen, W.L., Maxwell, D.S., Tirado-Rives, J., 1996. Development and testing of the OPLS all-atom force field on conformational energetics and properties of organic liquids. *J. Am. Chem. Soc.* 118, 11225–11236. doi:10.1021/ja9621760.
- Kedzierski, M.A., 2013. Viscosity and density of aluminum oxide nanolubricant. *Int. J. Refrig.* 36, 1333–1340. doi:10.1016/j.jrefrig.2013.02.017.
- Kedzierski, M.A., 2012. Viscosity and density of CuO nanolubricant. *Int. J. Refrig.* 35, 1997–2002. doi:10.1016/j.jrefrig.2012.06.012.

- Kedzierski, M.A., Brignoli, R., Quine, K.T., Brown, J.S., 2017. Viscosity, density, and thermal conductivity of aluminum oxide and zinc oxide nanolubricants. *Int. J. Refrig.* 74, 3–11. doi:[10.1016/j.ijrefrig.2016.10.003](https://doi.org/10.1016/j.ijrefrig.2016.10.003).
- Kioupis, L.L., Maginn, E.J., 1999a. Molecular simulation of Poly- α -olefin synthetic lubricants: impact of molecular architecture on performance properties. *J. Phys. Chem. B* 103, 10781–10790. doi:[10.1021/jp992399n](https://doi.org/10.1021/jp992399n).
- Kioupis, L.L., Maginn, E.J., 1999b. Rheology, dynamics, and structure of hydrocarbon blends: a molecular dynamics study of n-hexane/n-hexadecane mixtures. *Chem. Eng. J.* 74, 129–146. doi:[10.1016/S1385-8947\(99\)00053-4](https://doi.org/10.1016/S1385-8947(99)00053-4).
- Kirkpatrick, S., Gelatt, C.D., Vecchi, M.P., 1983. Optimization by simulated annealing. *Science* (80-) 220, 671–680. doi:[10.1126/science.220.4598.671](https://doi.org/10.1126/science.220.4598.671).
- Lin, L., Kedzierski, M.A., 2020. Data for: density and viscosity of a polyol ester lubricant: measurement and molecular dynamics simulation. Mendeley Data doi:[10.17632/vfskbn5sx6.1](https://doi.org/10.17632/vfskbn5sx6.1), v1.
- Liu, P., Yu, H., Ren, N., Lockwood, F.E., Wang, Q.J., 2015. Pressure-viscosity coefficient of hydrocarbon base oil through molecular dynamics simulations. *Tribol. Lett.* 60, 1–9. doi:[10.1007/s11249-015-0610-6](https://doi.org/10.1007/s11249-015-0610-6).
- Lu, J., Wang, Q.J., Ren, N., Lockwood, F.E., 2019. Correlation between pressure-viscosity coefficient and traction coefficient of the base stocks in traction lubricants: a molecular dynamic approach. *Tribol. Int.* 134, 328–334. doi:[10.1016/j.triboint.2019.02.013](https://doi.org/10.1016/j.triboint.2019.02.013).
- Maginn, E.J., Messerly, R.A., Carlson, D.J., Roe, D.R., Elliott, J.R., 2019. Best practices for computing transport properties 1. Self-diffusivity and viscosity from equilibrium molecular dynamics [Article v1.0]. *Living J. Comput. Mol. Sci.* 1, 1–20. doi:[10.33011/livecoms.1.1.6324](https://doi.org/10.33011/livecoms.1.1.6324).
- Marsh, K.N., Kandil, M.E., 2002. Review of thermodynamic properties of refrigerants + lubricant oils. *Fluid Phase Equilib.* 199, 319–334. doi:[10.1016/S0378-3812\(02\)00025-0](https://doi.org/10.1016/S0378-3812(02)00025-0).
- Martin, M.G., Siepmann, J.I., 1998. Transferable Potentials for Phase Equilibria. 1. United-Atom Description of n-Alkanes. *J. Phys. Chem. B* 102, 2569–2577. doi:[10.1021/jp972543+](https://doi.org/10.1021/jp972543+).
- Mayo, S.L., Olafson, B.D., Goddard, W.A., 1990. DREIDING: a generic force field for molecular simulations. *J. Phys. Chem.* 94, 8897–8909. doi:[10.1021/j100389a010](https://doi.org/10.1021/j100389a010).
- McCabe, C., Cui, S., Cummings, P.T., 2001. Characterizing the viscosity-temperature dependence of lubricants by molecular simulation. *Fluid Phase Equilib.* 183–184, 363–370. doi:[10.1016/S0378-3812\(01\)00448-4](https://doi.org/10.1016/S0378-3812(01)00448-4).
- McCabe, C., Manke, C.W., Cummings, P.T., 2002. Predicting the Newtonian viscosity of complex fluids from high strain rate molecular simulations. *J. Chem. Phys.* 116, 3339–3342. doi:[10.1063/1.1446045](https://doi.org/10.1063/1.1446045).
- Michels, H.H., Sienel, T.H., 2003. Refrigeration Lubricants- Properties and Applications. In: *Fuels and Lubricant Handbook: Technology, Properties, Performance, and Testing*. ASTM International, West Conshohocken, PA, USA, pp. 413–430.
- Mondello, M., Grest, G.S., Garcia, A.R., Silbernagel, B.C., 1996. Molecular dynamics of linear and branched alkanes: simulations and nuclear magnetic resonance results. *J. Chem. Phys.* 105, 5208–5215. doi:[10.1063/1.472363](https://doi.org/10.1063/1.472363).
- Plimpton, S., 1995. Fast parallel algorithms for short-range molecular dynamics. *J. Comput. Phys.* 117, 1–19. doi:[10.1006/jcph.1995.1039](https://doi.org/10.1006/jcph.1995.1039).
- Pluhackova, K., Morhenn, H., Lautner, L., Lohstroh, W., Nemkovski, K.S., Unruh, T., Böckmann, R.A., 2015. Extension of the LOPLS-AA force field for alcohols, esters, and monoolen bilayers and its validation by Neutron scattering experiments. *J. Phys. Chem. B* 119, 15287–15299. doi:[10.1021/acs.jpcc.5b08569](https://doi.org/10.1021/acs.jpcc.5b08569).
- Polak, E., Ribiere, G., 1969. Note sur la convergence de méthodes de directions conjuguées. *Rev. française d'informatique Rech. opérationnelle. Série rouge* 3, 35–43. doi:[10.1051/m2an/196903R100351](https://doi.org/10.1051/m2an/196903R100351).
- Press, W.H., Teukolsky, S.A., Vetterling, W.T., Flannery, B.P., 1988. *Numerical Recipes in C, Ch. 15.5, Nonlinear Models*. Cambridge University Press.
- Robertson, M.J., Tirado-Rives, J., Jorgensen, W.L., 2015. Improved peptide and protein torsional energetics with the OPLS-AA Force Field. *J. Chem. Theory Comput.* 11, 3499–3509. doi:[10.1021/acs.jctc.5b00356](https://doi.org/10.1021/acs.jctc.5b00356).
- Shinoda, W., Shiga, M., Mikami, M., 2004. Rapid estimation of elastic constants by molecular dynamics simulation under constant stress. *Phys. Rev. B* 69, 134103. doi:[10.1103/PhysRevB.69.134103](https://doi.org/10.1103/PhysRevB.69.134103).
- Siepmann, J.I., Karaborni, S., Smit, B., 1993. Simulating the critical behaviour of complex fluids. *Nature* 365, 330–332. doi:[10.1038/365330a0](https://doi.org/10.1038/365330a0).
- Siu, S.W.I., Pluhackova, K., Böckmann, R.A., 2012. Optimization of the OPLS-AA Force Field for Long Hydrocarbons. *J. Chem. Theory Comput.* 8, 1459–1470. doi:[10.1021/ct200908r](https://doi.org/10.1021/ct200908r).
- Sugii, T., Ishii, E., Müller-Plathe, F., 2015. Solubility of Carbon Dioxide in Pentaerythritol Hexanoate: molecular Dynamics Simulation of a Refrigerant-Lubricant Oil System. *J. Phys. Chem. B* 119, 12274–12280. doi:[10.1021/acs.jpcc.5b06459](https://doi.org/10.1021/acs.jpcc.5b06459).
- Verlet, L., 1967. Computer “Experiments” on Classical Fluids. I. Thermodynamical Properties of Lennard-Jones Molecules. *Phys. Rev.* 159, 98–103. doi:[10.1103/PhysRev.159.98](https://doi.org/10.1103/PhysRev.159.98).
- Wang, X., Sun, Y., Kang, K., 2015. Experimental investigation for the solubility of R1234ze(E) in pentaerythritol tetrahexanoate and pentaerythritol tetraoctanoate. *Fluid Phase Equilib.* 400, 38–42. doi:[10.1016/j.fluid.2015.05.008](https://doi.org/10.1016/j.fluid.2015.05.008).
- Youbi-Idrissi, M., Bonjour, J., Marvillet, C., Meunier, F., 2003. Impact of refrigerant-oil solubility on an evaporator performances working with R-407C. *Int. J. Refrig.* 26, 284–292. doi:[10.1016/S0140-7007\(02\)00129-9](https://doi.org/10.1016/S0140-7007(02)00129-9).
- Zhang, Y., Otani, A., Maginn, E.J., 2015. Reliable Viscosity Calculation from Equilibrium Molecular Dynamics Simulations: a Time Decomposition Method. *J. Chem. Theory Comput.* 11, 3537–3546. doi:[10.1021/acs.jctc.5b00351](https://doi.org/10.1021/acs.jctc.5b00351).